Validation of the Extended Simultaneous Kinetics and Ringdown Model by Measurements of the Reaction $NH_2 + NO$

G. Friedrichs,* M. Colberg, M. Fikri, Z. Huang, J. Neumann, and F. Temps

Institut für Physikalische Chemie, Olshausenstr. 40, Christian-Albrechts-Universität zu Kiel, D-24098 Kiel, Germany

Received: February 18, 2005; In Final Form: April 8, 2005

The determination of rate constants for fast chemical reactions from nonexponential cavity ringdown profiles requires a consideration of the interfering laser bandwidth effect that arises if the line width of the ringdown probe laser exceeds the absorption line width of the detected species. The deconvolution of the kinetics and the bandwidth effect can be accomplished with the extended simultaneous kinetics and ringdown (eSKaR) model presented by Guo et al. (Guo, et al. *Phys. Chem. Chem. Phys.* **2003**, *5*, 4622). We present a detailed validation of this eSKaR model by a corresponding investigation of the well-known rate constant for the reaction $NH_2 + NO$. Line profiles of the pulsed ringdown probe laser and the NH_2 absorption line were determined from forward modeling of experimental ringdown profiles and verified by narrow-bandwidth laser absorption measurements. In addition, the rate constant for the title reaction was evaluated using the eSKaR model and also by means of a conventional pump−probe approach with variable time delays between the photolysis (pump) and ringdown (probe) laser pulses. The resulting room temperature rate constant for the $NH_2 + NO$ reaction, $k_1 = (8.5 \pm 1.0) \times 10^{12}$ cm^3 mol^{-1} s^{-1}, and the room temperature pressure broadening coefficient of NH_2, $\Delta\nu_p^\circ = 2.27$ GHz/bar, measured on the $\tilde{A}^2A_1 \leftarrow \tilde{X}^2B_1$ transition at wavelengths around $\lambda = 597$ nm, were found to be in excellent agreement with the available literature data.

1. Introduction

Cavity ringdown spectroscopy (CRDS) is a highly sensitive and quantitative detection method that has been used to measure absorption spectra of numerous gas phase transient species.[1−3] Until recently, the kinetic applications of CRDS were limited to relatively slow reactions with lifetimes of the measured species longer than the ringdown time. In this case, the concentration of the reactive species remains almost constant during the ringdown period and complete concentration−time profiles can be obtained from the single-exponential ringdown time constants by pump−probe schemes with variable time delays between the photolysis (pump) and ringdown (probe) laser pulses. Practical examples of this "slow reaction" case include studies in the IR,[4,5] VIS,[6−8] and UV spectral regions.[9,10] For "fast reactions" that occur on the same time scale as the ringdown, the ringdown becomes nonexponential due to the convolution with the concentration change caused by the reactions. In this case, rate constants can be extracted from the nonexponential ringdown signals by the simultaneous kinetics and ringdown (SKaR) model developed by Brown et al.[11] As a test for their method, Brown et al. measured first-order loss and production reactions of NO_3. As required for this model, the line width of the detection laser used in their experiments was smaller than the absorber line width. In the meantime, the SKaR model has been also successfully applied for monitoring fast transients of CH radicals and N_2^+ ions in plasma discharges.[12,13]

However, nonexponential ringdown signals are also obtained in the absence of a reaction when the probe laser line width, $\Delta\nu_{laser}$, is comparable to or exceeds the absorption line width, $\Delta\nu_{abs}$, of the detected species.[14−18] This is a common situation when detecting small radicals with "conventional" pulsed dye lasers which are widely used in pulsed CRDS experiments. In this case, different frequency components of the probe laser light in the ringdown cavity experience different absorptions and thus decay with different time constants. The resulting ringdown exhibits multiexponential behavior even without convoluted kinetics (bandwidth effect).

We recently presented an extended version (eSKaR)[19] of the SKaR model of Brown et al.[11] to extract values of the rate constants of fast reactions from nonexponential ringdown profiles by deconvolution of the ensuing reaction and the bandwidth effect. For a precise determination of the rate constant by the eSKaR model, one has to know the line profiles of the absorption line and the probe laser. We first applied the eSKaR model in a study of the reaction of silylene with molecular oxygen, $SiH_2 + O_2 \rightarrow$ products.[19] The SiH_2 radicals were detected at a wavelength of $\lambda = 582.336$ nm by means of a pulsed dye laser with a bandwidth (FWHM) of $\Delta\nu_{laser} = 2.49$ GHz, which was roughly 2 times broader than the room temperature Doppler width of the SiH_2 absorption line, $\Delta\nu_D = 1.15$ GHz. The obtained value for the rate constant of the $SiH_2 + O_2$ reation was in fair agreement with the results of the only preceding direct study of that reaction by Chu et al.[20] This comparison, however, cannot be taken as the desirable critical assessment of the eSKaR model before a regular use. Such a validation should be based on corresponding measurements of the rate constant for a well-established reaction.

In this paper, we present a detailed assessment of the eSKaR model by measurements of the rate constant for the reaction

$$NH_2 + NO \rightarrow \text{products} \qquad \text{(R1)}$$

Reaction R1 was chosen for several reasons:

* Corresponding author. E-mail: gfriedr@phc.uni-kiel.de.

10.1021/jp0508599 CCC: $30.25
Published on Web 05/06/2005

(i) It has been extensively studied in numerous laboratories because of its great importance for NO_x removal in combustion processes,[21−23] so that its rate constant is well-known.

(ii) The reaction can be measured using CRDS over a wide range of $[NO]/[NH_2]$ excess ratios both by conventional pump−probe experiments with variable time delays between the pump (NH_2 generation by NH_3 photolysis) and probe (ringdown) laser pulses at relatively low $[NO]/[NH_2]$ excess ratios and by eSKaR experiments at rather high $[NO]/[NH_2]$ excess ratios. These measurements of the rate constant in the same experimental apparatus with two different measurement schemes provide a critical consistency check.

(iii) The rate constant for reaction R1 exhibits no significant pressure dependence at room temperature for pressures up to 1 bar.[8,24] Thus, observed changes in the nonexponential ringdown signals obtained at higher total pressures compared to the ringdown at the same NO excess ratio at lower pressures should be indicative of different contributions of the bandwidth effect (as a result of increased pressure broadening of the absorption line). Measurements of the rate constant at different pressures therefore assess the bandwidth related part of the eSKaR model. The measured line width parameters using a conventional "broad" pulsed dye laser as the ringdown probe laser can be compared to results obtained using a narrow single mode *cw* dye laser system at high resolution.

The experiments presented in this paper can be divided into four steps: (i) The probe laser bandwidth and line shape are determined by a forward modeling of experimental line profiles obtained at low pressures taking the bandwidth effect explicitly into account. (ii) Using the same forward modeling procedure, the pressure broadening coefficient of NH_2 is determined from line profile measurements at pressures up to $p = 1$ bar. These data, which depend on the previously determined laser bandwidth, are verified by direct narrow-bandwidth absorption measurements using a *cw* ring-dye laser system. (iii) The eSKaR model is applied to measure the rate constant for reaction R1 at pressures in the range 100 mbar $\leq p \leq$ 600 mbar. (iv) The obtained rate constant is checked by conventional pump−probe experiments.

2. eSKaR Model

In this section, the concepts of the extended simultaneous kinetics and ringdown (eSKaR) model and its use to extract fast rate constants from nonexponential ringdown signals are summarized. The terminology used stems from the paper of Brown et al.[11] and our previous paper.[19]

The decay of the laser light intensity, I, in the ringdown cavity can be described by the simple differential equation

$$\frac{dI_i}{I_i} = -(c\alpha_i + 1/\tau_0)\, dt \tag{1}$$

with c being the speed of light, α the absorption coefficient, and τ_0 the "empty cavity" decay constant which is measured without absorber in the cavity. τ_0 is defined in the usual way according to $\tau_0 = L/(c(1 - R))$, where L is the cavity mirror spacing and R accounts for reflection and scattering losses of the cavity mirrors and thus is mainly determined by the reflectivity of the mirrors. In general, the probe laser pulse excites multiple longitudinal and transverse cavity modes, i, which have to be taken into account separately. Equation 1 can be easily solved if a time-independent absorption coefficient is assumed. Then, each cavity mode, i, decays according to

$$I_i(t) = I_{i0} \exp\left(-c\alpha_i t - \frac{t}{\tau_0}\right) \tag{2}$$

In the case $\Delta\nu_{laser} < \Delta\nu_{abs}$, the mode index, i, can be omitted and the well-known single-exponential ringdown formula with a time constant of $1/\tau = 1/\tau_0 + c\alpha$ is recovered. However, generally speaking, the total intensity, $I(t)$, seen by the detector is given by the sum over all modes, i, excited within the cavity.

$$I(t) = \sum_i I_i(t) = e^{-t/\tau_0} \sum_i I_{i0} \exp(-\alpha_i t) \tag{3}$$

Equation 3 constitutes the multiexponential ringdown which is observed when the detection laser bandwidth, $\Delta\nu_{laser}$, is comparable to or even exceeds the absorber bandwidth, $\Delta\nu_{abs}$ (bandwidth effect).

For a time-dependent absorption, $\alpha(t)$, the integration of eq 1 yields

$$I_i(t) = I_{i0} \exp\left(-c\int_0^t \alpha_i(t)\, dt - \frac{t}{\tau_0}\right) \tag{4}$$

Next to the most important case of a (pseudo) first-order loss reaction, which is discussed in this paper, other cases such as first-order production and consecutive first-order production/first-order loss reactions also provide analytical solutions of eq 4.[11] For a more general numerical integration procedure, we refer to the paper of Macko et al.[5] For a (pseudo) first-order loss reaction with a rate constant, k, and $\alpha_i(t) = \alpha_{i0} \exp(-kt)$, the summation over all modes yields the complete ringdown signal.

$$I(t) = e^{-t/\tau_0} \sum_i I_{i0} \exp\left(-\frac{c\alpha_{i0}}{k}(1 - e^{-kt})\right) \tag{5}$$

For the derivation of eqs 3 and 5, the different frequency components have been assumed to decay with the same empty cavity decay constant, τ_0. In contrast to longitudinal modes, different excited transverse modes presumably decay with slightly different decay constants mostly due to spatially varying defects in the mirror surfaces and to their finite size causing a more or less multiexponential ringdown decay even for empty cavities.[25] In practice, however, adequate single-exponential ringdown signals are readily achieved by mode matching of the laser beam to the fundamental mode of the ringdown cavity by means of a telescope and by careful mirror alignment. Moreover, if a mode matching telescope setup is used, the mode structure will be dominated by the longitudinal modes of the fundamental transverse mode (TEM_{00}), and a summation over these longitudinal modes represents a good approximation. In most practical cases, if the cavity is not too short, the mode spacing will be small compared to the absorption and probe laser line widths (in our case, $\Delta\nu = 153$ MHz) and the summation extends over a large number of modes. Moreover, all modes are significantly broadened due to the pulsed excitation of the cavity[15,26] and inevitable shot-to-shot cavity length fluctuations in combination with the averaging of the ringdown signal induce a further blurring of the effective mode spectrum.[27] All these reasons contribute to an insensitivity of the calculated ringdown to the particular cavity mode spectrum

assumed, and consequently, in most cases, the discrete summations in eqs 3 and 5 can be safely replaced by a numerical integration.

The final form of eq 5 which is used to fit the experimental data is the so-called *Ratio*(*t*) function, which is the ratio of the ringdown measured with absorber to the ringdown measured with an empty cavity (or measured off-resonance).[19]

$$Ratio(t) = \frac{I(t)}{I_0 \exp(-t/\tau_0)} = \sum_i g_{laser}(\nu_i - \nu_c) \times \exp\left(-\frac{c\alpha_{c0} g_{abs}(\nu_i - \nu_c)}{k}(1 - e^{-kt})\right) \quad (6)$$

Here, $g_{laser}(\nu_i - \nu_c)$ and $g_{abs}(\nu_i - \nu_c)$ are the suitably normalized laser and absorption line shape functions, respectively. Essentially, eq 6 describes the convolution of the empty cavity ringdown with the kinetics and the bandwidth effect. If the line shape functions g_{laser} and g_{abs} are known from independent experiments, the only two remaining fit parameters are the first-order rate constant, k, and the (narrow-bandwidth) absorption coefficient, α_{c0}, at line center and at $t = 0$. Of course, the final parameters also critically depend on the line shape functions g_{laser} and g_{abs} assumed. It is one of the main issues of this paper to demonstrate that these line width effects can be properly taken into account. It will turn out that the resulting pseudo-first-order rate constant, k, is rather insensitive to line shape peculiarities.

3. Experimental Section

3.1. CRD Measurements. The cavity ringdown setup used in the present study was identical to that described in our previous paper.[19] Briefly, a 1 m long resonant optical cavity was formed by two highly reflective mirrors with 6 m radii of curvature. The measured empty cavity ringdown times, τ_0, were typically around 33 μs, corresponding to a 10 km light path. A Nd:YAG pumped tunable dye laser (Quanta Ray PDL-3) with a pulse duration of ≈9 ns was used as the ringdown probe laser. To reduce the number of excited transverse modes, the laser beam was shaped and spatially filtered by two telescopes and a 50 μm pinhole before it was injected into the cavity. The ringdown was monitored by a photomultiplier tube, and the signal was amplified, low-pass-filtered at 10 MHz, and stored in a digital storage oscilloscope with summed averaging (LeCroy 9362C, 1 GS/s, 8 bit vertical resolution). On one hand, the time response of ≈0.1 μs of the amplifier/filter combination used was kept sufficiently fast to resolve the convoluted concentration change but slow enough to average out longitudinal and transverse mode beating fringes superimposed on the ringdown signal,[15,25,26] which would have complicated the data evaluation. These interference effects, which could be clearly observed when using a fast 1 GHz detector, almost exclusively exhibit beating frequencies at a longitudinal mode spacing frequency of 153 MHz and the respective higher harmonics.[28]

Line shape measurements were performed by repeatedly scanning the wavelength over the absorption feature with a step size of ≈450 MHz. The decay constants, τ, were determined from the measured ringdown curves using a Levenberg−Marquardt nonlinear least-squares fitting routine. The first 0.3 μs of the ringdown, which could be affected by an oscillation ringing of the detection electronics, were excluded, and the fit was always restricted to the region $1 \geq I/I_0 \geq 0.85$ in order to reduce bandwidth effect related distortions of the observed spectral line shapes. Small scan-to-scan wavelength inaccuracies of the measured spectra due to the mechanical clearance of the grating were corrected by slightly off-setting the observed absorption peaks to a collective maximum in a postprocessing step.

For the kinetic measurements by means of the eSKaR method, the laser was step-scanned over a single NH_2 rovibronic absorption line and the complete ringdown signals were stored. The ringdown corresponding to the maximum absorption was taken as the on-resonance ringdown, whereas an off-resonance CRD signal was taken as a measure for the empty cavity ringdown. In this way, changes in the wavelength-independent background losses in the cavity and remaining diminutive deviations of the empty cavity decay from the expected single-exponential behavior were automatically included.

An ArF excimer laser (Lambda Physik Compex 102, ≈15 ns pulse duration) was used to generate NH_2 radicals by photolysis of NH_3 at $\lambda = 193$ nm. A delay generator (Stanford Research DG235) was used to control the triggers of the oscilloscope and the lasers, which were operated at a 10 Hz repetition frequency. To increase the spatial overlap between the photolysis and probe lasers, the photolysis beam was passed through the reaction cell at an angle of 20° with respect to the cavity axis, resulting in an effective single absorption path length of $l \approx 8.8$ cm.

3.2. Narrow-Bandwidth *cw* Laser Absorption Measurements. Another experimental setup was used to perform line shape measurements by means of narrow-bandwidth laser absorption. In these experiments, a Nd:YVO_4 solid-state laser (Coherent Verdi-V10) pumped *cw* ring-dye laser (Coherent 899-21) was used as the probe laser. The nominal bandwidth of this single mode laser was 100 kHz with a long-term frequency drift of 100 MHz/h, thus providing a light source with a line width much smaller than the absorption line. The photolysis of 700 ppm NH_3/argon mixtures was performed collinearly with the detection laser beam by slightly focusing the output of an ArF excimer laser (Lambda Physik EMG100, $\lambda = 193$ nm, $E = 90$ mJ/pulse, 1.4 Hz repetition frequency) into a 45 cm long flow cell. NH_2 detection was accomplished by a difference amplification scheme using two photodiodes. The time-resolved absorption signal was fed into two boxcar integrators (Stanford Research SR250) with the first gate set to a time before the photolysis (baseline subtraction) and the second gate set to a time delay of 100 μs relative to the excimer laser pulse. Complete spectral line shapes were obtained by slowly tuning the frequency of the probe laser over a scan range of 15 GHz (1.5 GHz/min). The output of the boxcar averager and the normalizing total intensity signal, I_0, were stored in an 8-bit digital oscilloscope, which was synchronized with the scanning Brewster plate of the dye laser. Typically, five consecutive scans were averaged in the oscilloscope. The scan range was checked against the relative wavelength offset measured by a wavemeter (MetroLux WL200) with an accuracy of 200 MHz, which in turn was calibrated using the spectrum of an iodine cell.

3.3. Gas Mixtures. Gas mixtures of typically 10% NO in argon and 10% NH_3 in argon were prepared manometrically and were stored in a stainless steel mixing cylinder and a glas flask, respectively. The gas reservoirs and the gas handling manifold could be evacuated to pressures of $p < 1 \times 10^{-4}$ mbar. The actual reaction mixtures with the desired [NO]/[NH_3] excess ratios were prepared from the high concentration mixtures and were further diluted with argon by using a flow system with calibrated mass flow controllers (Aera, FC series). The total pressure in the ringdown cavity, measured using capacitance manometers (MKS 622A), was varied in the range 2.5 mbar ≤ p ≤ 1000 mbar. The flow speed in the reactor was kept fast

enough to avoid repeated photolysis of the same gas volume. The gases and chemicals used were Ar (99.999%), which served as the inert carrier gas, NH_3 (99.99%), and NO (99.5%). The NO sample was further purified by trap-to-trap distillation before mixture preparation.

4. Results and Discussion

NH_2 radicals were generated by excimer laser photolysis at $\lambda = 193$ nm.

$$NH_3 + h\nu \rightarrow NH_2 + H$$

On the basis of the high resolution UV absorption spectrum reported by Chen et al.,[31] a photolysis center wavelength of $\lambda = 193.3$ nm, an excimer laser bandwidth of 0.5 nm (FWHM, Gaussian line shape), and a quantum yield of $\phi = 1$, the effective photolysis cross section of ammonia can be calculated to be $\sigma(NH_3) = 1.1 \times 10^7$ cm^2/mol (base e). With a typical concentration of $[NH_3]_0 = 7.5 \times 10^{-10}$ mol cm^{-3}, an average photolysis energy of $E = 40$ mJ/pulse, and a photolysis beam cross section of 1.5×3.0 cm^2, the initial NH_2 concentration in the reactor can be estimated to be $[NH_2]_0 = 1.1 \times 10^{-10}$ mol cm^{-3}.

Due to a slow rovibrational relaxation of the initially formed excited NH_2 radicals, a time delay was introduced between firing the photolysis laser and the probe laser in all experiments in order to ensure a quasi-steady-state NH_2 concentration (spectra measurements) and simple first-order kinetics (kinetic measurements), respectively. On the basis of measured NH_2 transients without NO in the reactor, this delay was chosen to vary from 200 μs at 10 mbar to 40 μs at 100 mbar to 5 μs at a total pressure of $p = 600$ mbar.

NH_2 was detected in the $\tilde{A}^2A_1(090) \leftarrow \tilde{X}^2B_1(000)\Sigma$ band at wavelengths around $\lambda \approx 597$ nm. Line shape measurements were performed by a high resolution scan over the isolated F_1 component of the $^PQ_{1,N}(6)$ transition at $\lambda = 597.676$ nm and the partially resolved spin-rotation doublet line $^PQ_{1,N}(7)$ at a center wavelength of $\lambda = 597.375$ nm. For the latter line, on the basis of measurements of Kohse-Höinghaus et al.,[32] the doublet splitting was set to a value of 3.44 GHz and the intensity ratio, which was partly used as an adjustable parameter, was kept at values around 0.82.

For quantitative concentration and line shape measurements, it was important to avoid saturation of the absorber within the ringdown cavity. A quick estimate of the degree of saturation is possible by a comparison of the excitation rate of the absorber with the relaxation rate of the upper level, which is dominated by collisional quenching.[29] For the experimental conditions used in this work, even at the lowest pressure $p = 2.5$ mbar, the excitation rate was roughly 3 orders of magnitude smaller than the corresponding fluorescence quenching rate 9.3×10^6 s^{-1} reported by Halpern et al.[30] Consequently, saturation could be ruled out and no indications for saturation broadening were found in the measured line profiles.

4.1. Probe Laser Bandwidth. The bandwidth and the line shape of the ringdown probe laser were determined from high resolution CRD scans over NH_2 absorption lines at total pressures of 2.5 mbar $\leq p \leq$ 10 mbar. Provided that the CRD spectra are not distorted by the laser bandwidth effect, at these low pressures, the shape of the observed spectral lines can be described by the convolution of the probe laser line shape with the purely Doppler broadened NH_2 absorption line. At an experimental temperature of $T = 295$ K, the Doppler width (FWHM) of $\Delta\lambda = 1.84 \times 10^{-3}$ nm ($\Delta\nu = 1.54$ GHz) is much larger than the expected natural line width of 10−100 MHz. In the subsequent data treatment, this minor contribution of the natural line width to the absorption line width was neglected.

Even if the evaluation of a multiexponential ringdown is restricted to very short decay times, the measured CRD line shape may be somewhat distorted due to the bandwidth effect. Therefore, we explicitly took the bandwidth effect into account by performing a forward fitting procedure similar to the forward modeling described by Wachsmuth and Abel.[33] To model the observed line profile, the probe laser center wavelength was numerically step-scanned across the absorption line. For each center wavelength position, a complete ringdown was calculated on the basis of eq 3 by assuming a reasonable trial probe laser line shape. These numerically constructed ringdown signals were processed in the same way as the experimental ringdown profiles have been processed during the CRD spectra acquisition. In our case, the first 0.3 μs of the ringdown were excluded and the nonlinear fit of the ringdown was restricted to the region $1 \geq I/I_0 \geq 0.85$. In this way, an emulated CRD spectrum was calculated which could be compared with the experiment. The residuum was minimized using a Levenberg−Marquardt least-squares fitting routine, which was found to converge fast and reliably in all cases.

A careful inspection of the finally predicted ringdown decays revealed a good agreement with the *complete* experimental ringdown curves for not too large offsets of the probe laser center wavelength. Indications for ringdown anomalies associated with the longitudinal mode structure of the dye laser as reported by Hodges et al.,[16] which eventually would spoil the use of a simple functional form for the probe laser profile, were not found. If the probe laser center wavelength was set to the wings of the absorption line, however, the calculated ringdown signal deviated slightly from the experimental data at long decay times. At long decay times and in case of a sparse overlap of the absorption line with the probe laser line shape, the ringdown becomes very sensitive to line shape peculiarities. Although not critical with respect to the eSKaR method, these deviations show quite plainly the limitations of the forward fitting procedure with respect to line width measurements. Therefore, line shape measurements should be based on the beginning part of the ringdown decay rather than relying on the complete ringdown curve, since the expected distortions due to the bandwidth effect are small for the early fraction of the ringdown. For this reason, boxcar integrator based ringdown measurements with a rather long time delay between the two boxcar gates as used by Romanini and Lehmann[34] and Wachsmuth and Abel[33] are thought to be less precise in this case.

Figure 1 displays a high resolution scan over the well separated F_1 component of the $^PQ_{1,N}(6)$ line obtained at a total pressure of $p = 10$ mbar. The solid and dashed curves are based on the forward fitting procedure and correspond to simulated line profiles assuming a purely Doppler broadened absorption line shape and a Gaussian ($\Delta\nu_{laser} = 3.29$ GHz) and, alternatively, a Lorentzian ($\Delta\nu_{laser} = 3.67$ GHz) probe laser profile. Clearly, the Gaussian laser profile fails to reproduce the outer wings of the experimental line shape, whereas a simulation based on a Lorentzian laser profile provides a nearly perfect fit. Consequently, a Lorentzian laser line shape was assumed throughout this paper. It is important to determine the laser bandwidth and line shape at similar laser settings as used for the subsequent measurements, since both properties may depend on the wavelength, laser dye, and grating order used. For example, as we have reported in our previous paper and as it was confirmed again in this work, comparable SiH_2 measure-

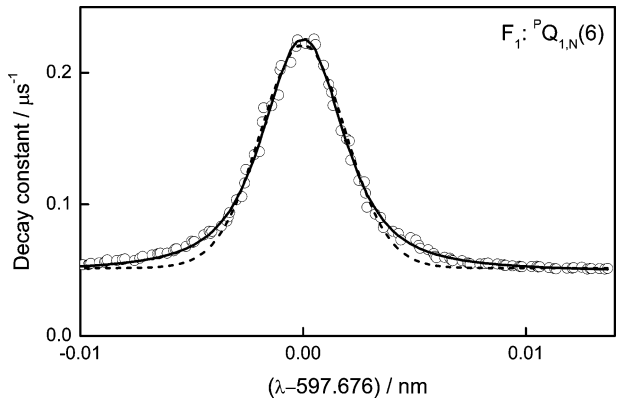

Figure 1. Forward modeling of laser line shape assuming a Lorentzian with $\Delta\nu_{laser} = 3.29$ GHz (—) and a Gaussian laser profile with $\Delta\nu_{laser} = 3.67$ GHz (- - -). Total pressure $p = 10$ mbar.

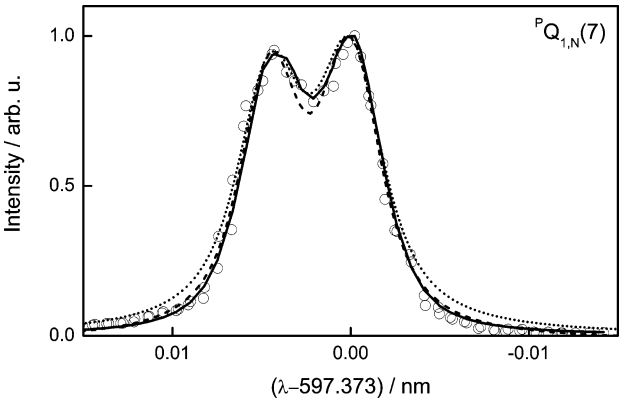

Figure 2. Influence of the bandwidth effect on the determination of the laser bandwidth: (—) forward fit taking into account the bandwidth effect with $\Delta\nu_{laser} = 3.00$ GHz; (- - -) direct fit neglecting the bandwidth effect with $\Delta\nu_{laser} = 2.64$ GHz; (• • •) "real" line shape with $\Delta\nu_{laser} = 3.00$ GHz. Total pressure $p = 2.5$ mbar.

ments using the same laser system but a different dye and grating order at wavelengths around $\lambda = 582$ nm could be better reproduced assuming a Gaussian laser profile.[19] On the other hand, both the laser bandwidth and line shape did not change significantly with extended use of any one dye sample.

A comparison of a line shape obtained by a direct fit procedure that neglects the bandwidth effect with the corresponding line shape based on a forward fit is given in Figure 2. Both the direct fit of the "double" $^PQ_{1,N}(7)$ line with $\Delta\nu_{laser} = 2.64$ GHz (dashed curve) and the forward fit with $\Delta\nu_{laser} = 3.00$ GHz (solid curve) agree reasonably well with the experiment. Eventually, the dotted curve in Figure 2 represents the experimental line shape which would have been observed without the bandwidth effect. Altogether, an apparent "spectral narrowing" of the experimental CRD line shape is observed which can be traced back to the fact that the bandwidth effect is more pronounced in the outer wings of the absorption line than at line center. However, such a spectral narrowing and a "spectral broadening" effect as reported by Wachsmuth and Abel[33] depend on the actual experimental conditions, for example, the laser and absorption line width, the overall absorption, and also the ringdown fitting procedure.

Overall, on the basis of 14 measurements, the laser line shape has been determined to be Lorentzian with a line width of

$$\Delta\nu_{laser} = (3.04 \pm 0.11)\ \text{GHz}$$

The stated error corresponds to the error of the mean based on a 2σ confidence level. Whichever subset of the data was taken, that is, the measurements at total pressures of 2.5 and 10 mbar or the measurements using the two different rotational lines, in each case an excellent agreement of the determined line widths within this error limit was obtained.

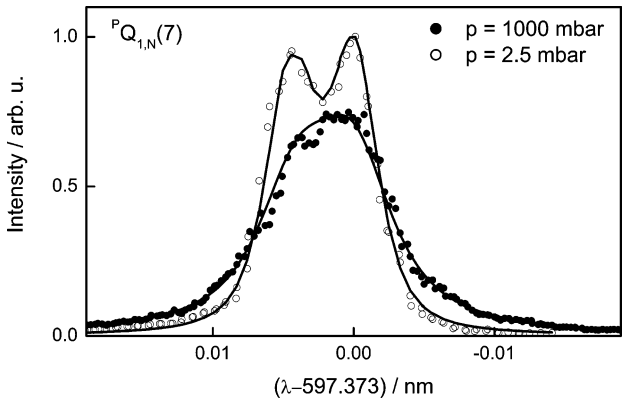

Figure 3. CRD measurement of NH_2 pressure broadening. The symbols refer to experiments at a total pressure of $p = 2.5$ mbar (○) and 1000 mbar (●). The solid curves represent the corresponding simulations with a pressure broadening of $\Delta\nu \approx 0$ and 2.28 GHz, respectively, obtained from a forward modeling of the $^PQ_{1,N}(7)$ absorption line (see text).

4.2. Pressure Broadening of NH_2. The pressure broadening coefficient, $\Delta\nu_p$, of NH_2 in argon was determined at pressures up to 1000 mbar by means of (i) CRDS using the pulsed dye laser system with $\Delta\nu_{laser} = 3.04$ GHz and (ii) narrow-bandwidth *cw* laser absorption using a dye laser with an effective bandwidth of $\Delta\nu_{laser} < 100$ MHz.

4.2.1. CRD Measurements. In the CRD measurements, the pressure broadening coefficient, $\Delta\nu_p$, was determined from high resolution scans of the F_1:$^PQ_{1,N}(6)$ and $^PQ_{1,N}(7)$ lines at total pressures of $p = 100$, 300, 600, and 1000 mbar. Typically, each experimental line profile, as the one shown in Figure 3, constitutes the average of six single scans and, moreover, each experiment was repeated three times. The two line profiles of the $^PQ_{1,N}(7)$ spin-rotation doublet line shown in Figure 3 were measured at $p = 2.5$ mbar and $p = 1000$ mbar, respectively. The disappearance of the doublet structure of the line at a pressure of $p = 1000$ mbar reveals a rather strong pressure broadening effect. The pressure broadening coefficient, which was determined by applying the forward fitting procedure described in section 4.1, is plotted as a function of the total pressure in Figure 4. The error bars account for the combined errors of the mean (2σ) and the laser bandwidth, as determined in section 4.1. Even though the pressure broadening measured for the $^PQ_{1,N}(6)$ line (filled circles) appears to be marginally higher than the data based on the $^PQ_{1,N}(7)$ line profiles (open circles), within the error limits, all data are nicely represented by the straight solid line, which yields a pressure broadening coefficient of

$$\Delta\nu_p = (2.39 \pm 0.25)\ \text{GHz/bar}$$

where the error limit is given by the 2σ error of the weighted linear regression. As expected, the axis intercept is essentially zero, since the natural line broadening is small and it also implicitly entered into the laser bandwidth (see section 4.1).

4.2.2. Narrow-Bandwidth Absorption Measurements. To verify the CRD measurements that rely on an accurate value of the laser bandwidth and on the applicability of the forward fitting procedure, additional narrow-bandwidth laser absorption measurements of the pressure broadening have been performed.

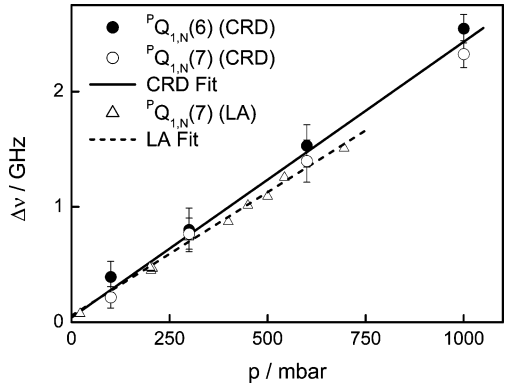

Figure 4. Pressure broadening of the $^{P}Q_{1,N}(6)$ and $^{P}Q_{1,N}(7)$ absorption lines measured by means of cavity ringdown (CRD) and narrow-bandwidth laser absorption (LA). The symbols refer to experimental data as indicated in the key. The slopes of the lines correspond to pressure broadening coefficients of $\Delta\nu_p = 2.39$ GHz/bar (—, CRD measurements) and 2.14 GHz/bar (- - -, LA measurements), respectively.

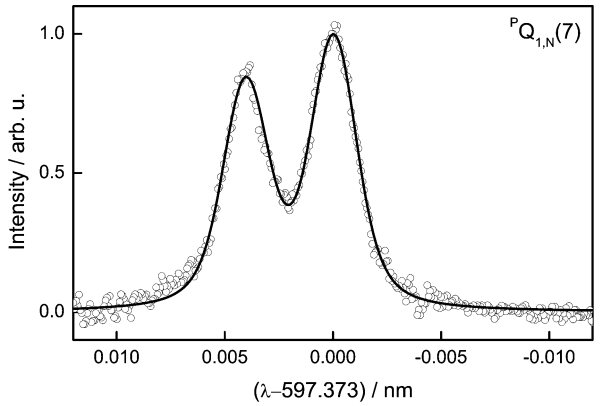

Figure 5. Narrow-bandwidth laser absorption measurement of NH_2 pressure broadening. The symbols refer to an experiment at a total pressure of $p = 450$ mbar, and the solid curve represents the corresponding Voigt fit of the $^{P}Q_{1,N}(7)$ absorption line exhibiting a pressure broadening of $\Delta\nu = 1.01$ GHz.

Here, the nominal bandwidth of the laser system was 100 kHz; however, an effective line width of 10−100 MHz might be reflected in the spectra due to long-term drift of the laser frequency during the line profile measurements. A typical line profile measured at a total pressure of $p = 450$ mbar is shown in Figure 5. Clearly, compared to the pulsed dye laser CRD measurements in Figure 3, the doublet structure of the $^{P}Q_{1,N}(7)$ line is much better resolved. The observed line profiles were directly fitted assuming a Voigt profile with the Gaussian width fixed to the value of the NH_2 Doppler broadening. The resulting Lorentzian widths from 13 measurements at pressures of 22 mbar $\leq p \leq$ 695 mbar are plotted as a function of pressure in Figure 4 as open triangles together with the CRD results. Again, a linear relationship holds (dashed line), yielding a pressure broadening coefficient of

$$\Delta\nu_p = (2.14 \pm 0.14)\ \text{GHz/bar}$$

Here, the error limit represents the 2σ error of the linear regression. In this case, the small positive intercept of 58 ± 52 MHz reflects contributions from both the natural line width and the finite bandwidth of the laser system.

4.2.3. Comparison. The experimental pressure broadening data obtained using cavity ringdown (CRD) and narrow-bandwidth laser absorption (LA) are compared in Figure 4. A high pressure extrapolation of the pressure broadening obtained from the narrow-bandwidth laser absorption measurements predicts a slightly lower value at 1000 mbar than is compatible with the CRD measurements. However, keeping in mind that the given error bars do not include additional systematic errors which may arise from baseline issues, scan interval inaccuracies and, in the case of the CRD measurements, from the forward fitting procedure itself, the agreement of the two data sets is very good. This shows that the bandwidth effect in the CRD measurements was properly taken into account. For comparison, a 27% higher pressure broadening coefficient of $\Delta\nu_p = (3.03 \pm 0.22)$ GHz/bar would have been obtained by using a direct fit of the observed line shapes instead of performing the forward fitting procedure. By all means accurate enough for the purpose of eSKaR measurements, these results again stress the importance of a reliable consideration of the line shape distortion effect when using cavity ringdown spectroscopy to measure absorption line widths.

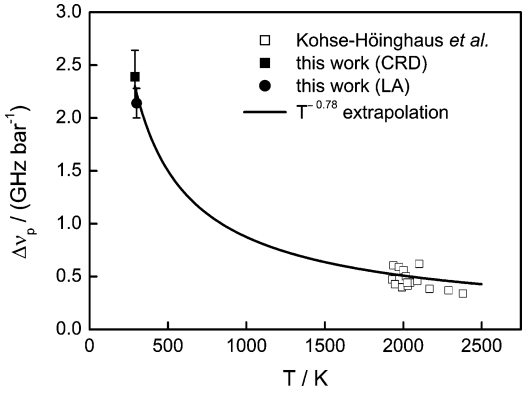

Figure 6. Pressure broadening coefficient, $\Delta\nu_p$, of NH_2 in argon: (■, ●) room temperature data of this work based on cavity ringdown (CRD) and laser absorption (LA) measurements; (□) high temperature data from Kohse-Höinghaus et al.;[32] (—) temperature-dependent fit.

The determined pressure broadening coefficients of NH_2 in argon can be compared to literature data. Kohse-Höinghaus et al.[32] investigated the pressure broadening of the $^{P}Q_{1,N}(7)$ line in argon at temperatures of 1800−2400 K at total pressures of 1, 2, and 4 atm. They performed shock tube experiments and generated NH_2 radicals by either photolysis or pyrolysis of mixtures of ammonia in argon with NH_3 mole fractions below 1%. Line profiles were measured using a narrow-bandwidth laser absorption system by rapidly scanning the laser frequency across the doublet line during reflected shock wave conditions. Their results are shown as a function of temperature (open squares) together with the cavity ringdown (filled square) and laser absorption (filled circle) results of this study in Figure 6. Kohse-Höinghaus et al. reported an average value of $\Delta\nu_p = 0.518$ GHz/bar at 2000 K. For the assumption of hard-sphere collisions, $\Delta\nu_p$ scales with $T^{-0.5}$; however, due to the commonly observed decrease of the collisional cross section with increasing temperature, a temperature exponent somewhat lower than −0.5 is expected. In Figure 6, the extrapolation of the room temperature data of the present work to the high temperature data (solid curve) yields a reasonable temperature exponent of −0.78 corresponding to the recommended relation

$$\Delta\nu_p = \Delta\nu_p^{\circ} \times (T/295\ \text{K})^{-0.78}$$

Here, $\Delta\nu_p^{\circ} = 2.27$ GHz/bar constitutes the average of the pressure broadening coefficients determined in this work.

4.3. Rate Measurements for the Reaction $NH_2 + NO$. The room temperature rate constant for the reaction $NH_2 + NO \rightarrow$ products (R1) was determined under pseudo-first-order condi-

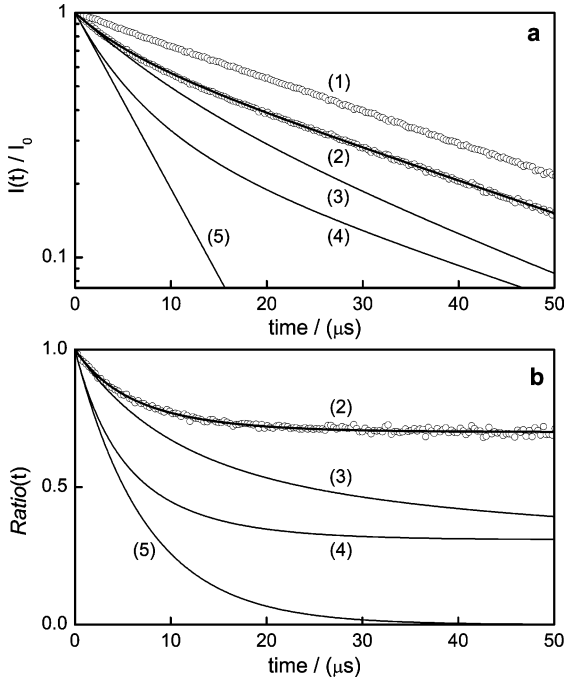

Figure 7. Influence of the kinetics and the laser bandwidth effect on experimentally observed ringdown signals (top panel) and *Ratio* functions (bottom panel) as used for an eSKaR evaluation: (1) without absorber (empty cavity/off-resonance); (2) with kinetics, with the bandwidth effect; (3) without kinetics, with the bandwidth effect; (4) with kinetics, without the bandwidth effect; (5) without kinetics, without the bandwidth effect. Experimental parameters: $\Delta\nu_{laser}/\Delta\nu_{abs} = 1.6$, $k^{-1} = 8.8$ μs, $\tau_0 = 33$ μs, and $\alpha_{c0} = 4.4 \times 10^{-6}$ cm^{-1}.

tions with NO as the excess species at pressures up to 600 mbar using two different experimental approaches: (i) the eSKaR approach at high [NO]/[NH_2] excess ratios with first-order rate constants, k', comparable with the empty cavity ringdown time constant, τ_0^{-1} (fast reaction case), and (ii) a conventional pump−probe approach with variable time delays between photolysis pump and ringdown probe laser at moderately high [NO]/[NH_2] excess ratios in order to realize a slow reaction case with $k' < \tau_0^{-1}$.

4.3.1. eSKaR Measurements. Figure 7 serves as an example of a typical eSKaR experiment and the corresponding data reduction procedure. The experimental ringdown is compared to an eSKaR fit as well as simulations of the same experiment neglecting the kinetics and/or the bandwidth effects. Semilogarithmic plots of the ringdown signals are depicted in Figure 7a. Curve 1 represents the single-exponential empty cavity ringdown signal which was measured off-resonance and was used to calculate the *Ratio* functions. Curve 2 was obtained on-resonance and was fitted by means of the eSKaR model. It clearly exhibits nonexponential character. In this experiment, with $\Delta\nu_{laser}/\Delta\nu_{abs} \approx 1.6$, a strong bandwidth effect is expected and also the kinetics takes place on the same time scale as the ringdown. Here, the inverse pseudo-first-order decay constant of $k^{-1} = 8.8$ μs is comparable to the empty cavity decay time of $\tau_0 = 33$ μs. On the basis of these data, curves 3−5 were calculated by neglecting the kinetics ($k \approx 0$, curve 3), by neglecting the bandwidth effect ($\Delta\nu_{laser} \approx 0$, curve 4), and also by neglecting both effects (curve 5). In all simulations, an absorption coefficient of $\alpha_{c0} = 4.4 \times 10^{-6}$ cm^{-1} has been assumed. Curve 3 as well as curve 4 strongly deviate from the eSKaR fit, which clearly indicates the importance of both the kinetics and the bandwidth effect.

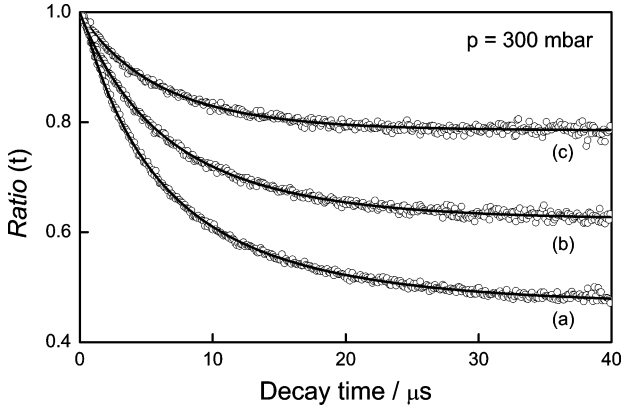

Figure 8. Experimental *Ratio*(*t*) curves at different concentrations of NO: (a) [NO] = 8.8×10^{-9} mol/cm^3; (b) 1.1×10^{-8} mol/cm^3; (c) 1.5×10^{-8} mol/cm^3. The experimental conditions are given in Table 1.

The corresponding *Ratio* functions shown in Figure 7b decrease at short ringdown times and reach plateau values for long reaction times. A consideration of the two limiting cases of the *Ratio* function with $t \rightarrow 0$ or $t \rightarrow \infty$

$$Ratio(t \rightarrow 0) = \sum_i g_{laser}(\nu_i - \nu_c) \exp(-c\alpha_{c0} g_{abs}(\nu_i - \nu_c)t) \quad (7)$$

$$Ratio(t \rightarrow \infty) = \sum_i g_{laser}(\nu_i - \nu_c) \exp\left(-\frac{c\alpha_{c0} g_{abs}(\nu_i - \nu_c)}{k}\right) \quad (8)$$

delivers insight in the interdependence of the fitting parameters. Supposing that the line shape functions g_{laser} and g_{abs} are known, the initial decrease is determined by the parameter α_{c0}, whereas the plateau value is determined by the ratio of α_{c0} over k. As can be seen from Figure 7b, when neglecting the kinetics (curve 3), the initial decrease is still well reproduced, whereas the resulting plateau value is much too low. The same holds for the comparison of curves 4 and 5, which would have been obtained using a narrow-bandwidth laser (no bandwidth effect). It is this partial decoupling of the parameters that makes the fit very stable and allows a reliable rate constant determination.

For the eSKaR measurements, the experimental conditions were chosen such that the high NO excess ratios of $66 \leq$ [NO]/[NH_2]$_0 \leq 700$ ensured first-order conditions and a fast reaction case with $k' \approx \tau_0^{-1}$. Four sets of data were obtained at pressures of $p = 100$, 200, 300, and 600 mbar. Figure 8 shows the *Ratio*(*t*) functions for three experiments at a total pressure of $p = 300$ mbar. With increasing NO concentration (curve a → curve c), higher plateau values are reached as is consistent with shorter NH_2 lifetimes at higher NO concentrations. In all cases, the experimental *Ratio*(*t*) curves could be nicely reproduced by the eSKaR model (eq 6) using α_{c0} and k' as the only adjustable parameters. The probe laser and absorption line width were set to the values given in sections 4.1 and 4.2.

The detailed results for the data set shown in Figure 8 are listed in Table 1. Although comparable [NH_2]$_0$ concentrations were used in all experiments, the obtained values for α_{c0} decrease with increasing NO concentrations due to a 15 μs delay set between the laser photolysis and the ringdown probe laser pulse. When extrapolating back to the photolysis time, coincident α_{c0}^0 values were derived. The average result, $\alpha_{c0}^0 = 2.44 \times 10^{-5}$ cm^{-1}, can be compared to an estimated absorption coefficient: on the basis of an extrapolated high temperature absorption cross section of the $^PQ_{1,N}(7)$ line taken from

TABLE 1: Pseudo-First-Order Rate Constants, k', and Absorption Coefficients, α_{c0}, from the Least-Squares Fits to the Obtained *Ratio*(*t*) Plots for the Experimental Data Set Shown in Figure 8[a]

[NO]/ (10^{-8} mol cm^{-3})	k'/ (10^5 s^{-1})	α_{c0}/ (10^{-6} cm^{-1})	α_{c0}^{0}[b]/ (10^{-5} cm^{-1})
0.88	0.63	8.95	2.29
1.00	0.90	7.08	2.74
1.13	0.97	5.70	2.44
1.25	1.14	4.41	2.44
1.37	1.24	3.61	2.32
1.50	1.33	3.27	2.40

[a] $T = (295 \pm 1)$ K, $p = 300$ mbar, $[NH_3] = 1.14 \times 10^{-9}$ mol/cm^3, buffer gas = Ar, photolysis energy $E \approx 24$ mJ/pulse. [b] Extrapolated back to the time of photolysis to account for the 15 μs time delay of the probe laser pulse.

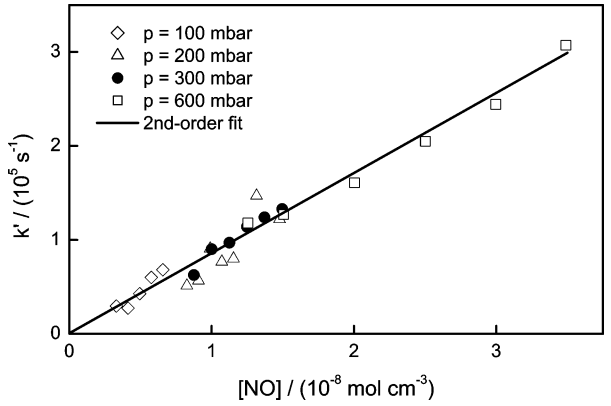

Figure 9. Pseudo-first-order rate constant, k', as a function of the concentration of NO at four different total pressures as indicated in the key. The line corresponds to a combined fit of all data with a second-order rate constant of $k = 8.53 \times 10^{12}$ cm^3 mol^{-1} s^{-1}.

Votsmeier et al.[35] and the measured intensity ratio of the $^{P}Q_{1,N}(6)$ and $^{P}Q_{1,N}(7)$ line, the (narrow-bandwidth) room temperature absorption cross section of the $^{P}Q_{1,N}(6)$ line could be estimated to $\sigma(NH_2, 300\ \text{mbar}) \approx 3.5 \times 10^6$ cm^2/mol. With $[NH_2]_0 \approx 9.7 \times 10^{-11}$ mol /cm^3, calculated from the initial ammonia concentration and the photolysis laser energy, an absorption coefficient of $\alpha_{c0}^{0} = 3.0 \times 10^{-5}$ cm^{-1} is obtained. Bearing in mind the uncertainty of such a rough estimation, the agreement of the experimental and estimated value within 20% is excellent.

A combined plot of all extracted pseudo-first-order rate constants against the NO concentration is shown in Figure 9. Here, different total pressures correspond to a different extent of the bandwidth effect ($1.25 < \Delta\nu_{laser}/\Delta\nu_{abs} < 1.82$). Since the reaction $NH_2 + NO$ is not expected to show any pressure dependence under the experimental conditions,[24] the obtained linear correlation over all experiments is another indication that the eSKaR model properly corrects for the bandwidth effect. A combined linear fit of all data yields the second-order rate constant of the reaction $NH_2 + NO$ at room temperature

$$k_1 = (8.53 \pm 0.70) \times 10^{12}\ \text{cm}^3\ \text{mol}^{-1}\ \text{s}^{-1}$$

where the error limit is given by the 2σ error of the linear regression. The axis intercept is essentially zero, indicating a negligible contribution of additional NH_2 loss processes.

With the data set at $p = 600$ mbar as an example, Figure 10 points out the influence of the bandwidth effect on the determined rate constant. Next to the eSKaR evaluation with $k = (8.4 \pm 1.1) \times 10^{12}$ cm^3 mol^{-1} s^{-1} for this single data set (squares), the results of two additional analyses (i) using the improper line width parameters from the direct fitting procedure (circles) and (ii) completely neglecting the bandwidth effect by setting the laser bandwidth to $\Delta\nu_{laser} < 150$ MHz (triangles) are given. In both cases, the deviation from the correct values decreases with increasing NO concentration. Obviously, at high NO excess ratios, the kinetics becomes the dominant effect. Neglecting the bandwidth effect, however, yields misleading rate constants at low excess ratios and an overall linear regression of the data points with $k = (5.8 \pm 2.2) \times 10^{12}$ cm^3 mol^{-1} s^{-1} results in a significantly lower second-order rate and a unreasonable high intercept. Interestingly enough, the wrong line shape model with a laser bandwidth too low by 12% and a pressure broadening coefficient too high by 27% (open circles) still produces a reasonable result of $k = (7.6 \pm 1.5) \times 10^{12}$ cm^3 mol^{-1} s^{-1}.

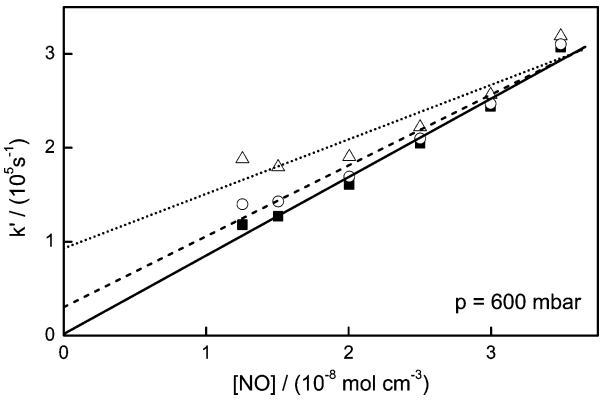

Figure 10. Pseudo-first-order rate constant, k', as a function of the concentration of NO at a total pressure of $p = 600$ mbar. The symbols and lines correspond to evaluations based on different line shape models: (—, ■) line widths based on forward fitting procedure; (- - -, ○) line widths based on (invalid) direct fit; (• • •, △) neglecting the bandwidth effect.

Altogether, this example again emphasizes the importance of a quantitative consideration of the bandwidth effect. However, peculiarities of the line shape model and with it small line width inaccuracies do not induce large errors in the determined rate constant. For example, a combined fit over all data based on the wrong line shape model as described above yielded a merely 4% lower value for the final rate constant.

4.3.2. Conventional Pump−Probe Measurements. For the measurements with variable time delays between photolysis pump and ringdown probe laser, the experimental conditions were chosen such that moderate NO excess ratios of $8 \le [NO]/[NH_2]_0 \le 14$ provided for a slow reaction case with $k' < \tau_0^{-1}$. In the upper plot of Figure 11, a typical experiment with $[NO]/[NH_2]_0 = 12$ at a total pressure of $p = 50$ mbar is shown. Absolute concentration profiles were calculated from the experimental $(1/\tau - 1/\tau_0)$ profiles, which were obtained by a single-exponential fit of the measured ringdown curves restricted to short decay times (see section 3). At overall low absorption, the difference $(1/\tau - 1/\tau_0)$ is proportional to the concentration of NH_2 according to

$$(1/\tau - 1/\tau_0) = c\sigma_{eff}[NH_2] \qquad (9)$$

Here, σ_{eff} is an effective absorption cross section that accounts for the effective overlap of absorption and probe laser line profile. However, detailed simulations of the ringdown curves using the forward modeling procedure described in section 4.1 showed that for the experimental conditions used in this study the signal intensity was already slightly distorted. σ_{eff} was found to decrease with increasing NH_2 concentration, and therefore,

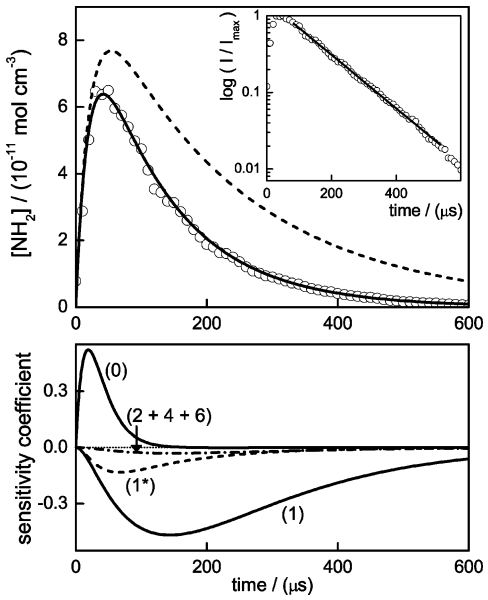

Figure 11. NH_2 concentration time profile and sensitivity analysis for an experiment at $T = 295$ K and $p = 50$ mbar, $[NH_3]_0 = 7.45 \times 10^{-10}$ mol/cm^3, $[NH_2^*]_0 = [H]_0 = 1.10 \times 10^{-10}$ mol/cm^3, $[NO]_0 = 1.03 \times 10^{-9}$ mol/cm^3. Upper panel: experimental NH_2 profile (○) and best fit (—). The dashed line refers to a simulation with $k_1(NH_2 + NO)$ reduced by a factor of 2. The inset graph shows a semilogarithmic plot of the same experiment along with a pseudo-first-order linear fit. Lower panel: Sensitivity analysis. (R0) $NH_2^* + M \rightarrow NH_2 + M$, (R1) $NH_2 + NO \rightarrow$ products, (R1*) $NH_2^* + NO \rightarrow$ products, (R2) $2NH_2 + M \rightarrow N_2H_4 + M$, (R4) $NH_2 + H + M \rightarrow NH_3 + M$, (R6) $NH_2 + OH \rightarrow NH_2OH$.

σ_{eff} was parametrized as a function of $(1/\tau - 1/\tau_0)$. At the highest concentrations used, σ_{eff} decreased by roughly 7% relative to the limiting low absorption value. Again, the required narrow-bandwidth absorption cross section of $\sigma(295\text{ K}, 50\text{ mbar}) = 5.8 \times 10^6$ cm^2/mol for the maximum of the $^PQ_{1,N}(7)$ doublet line was calculated from the high temperature absorption cross section reported by Votsmeier et al.[35]

In contrast to the eSKaR measurements, which were performed at very high [NO]/[NH_3] excess ratios of up to 700, the moderate excess ratio of ~10 used for the conventional pump−probe experiments is somewhat too small to ensure simple first-order kinetics. To model the slow formation of NH_2 and to assess the influence of possible secondary reactions, the simple reaction mechanism given in Table 2 was applied. The Chemkin-II chemical kinetics package[36] and a Levenberg−Marquardt least-squares fitting routine was used for numerical simulations. As it becomes clear from the initial increase of the NH_2 signal in Figure 11, NH_2 radicals are initially formed in rovibrationally excited states, and thus, allowance was made for an excited NH_2^* species. Supplement reactions of NH_2^* analogous to reactions R1−R7 are not listed in Table 2 but were also taken into account by assuming the same rate constant as that for the thermally equilibrated NH_2.

The experimental profiles were fitted using the rate of reaction R1, $NH_2 + NO$, the rate of the relaxation process (R0), $NH_2^* + M \rightarrow NH_2 + M$, and the initial concentration of NH_2^* as the free parameters. As exemplarily shown by the solid curve in the upper plot of Figure 11, all experiments could be nicely reproduced by the numerical simulation and resulted in a consistent rate data set. The dashed curve, which refers to a simulation with k_1 reduced by a factor of 2, illustrates the strong influence of the rate constant of k_1 on the simulated NH_2 profile.

The lower plot of Figure 11 depicts the results of a sensitivity analysis of the same experiment. Here, the sensitivity coefficient was normalized with respect to the maximum concentration of NH_2 over the time history. Whereas the initial increase of the NH_2 signal is clearly dominated by the relaxation process (R0), the signal decrease at reaction times >100 μs is predominantly due to reaction R1, $NH_2 + NO$. At intermediate reaction times, however, part of the amidogen radicals are also consumed by the reaction (R1*), $NH_2^* + NO$. The curve of the sum of the sensitivity coefficients of the next three most sensitive reactions R2, R4, and R6 (dash−dotted curve) makes it clear that all other secondary reactions play a minor role.

TABLE 2: Reaction Mechanism Used for the Evaluation of the Conventional Pump−Probe Measurements[a]

no.	reaction	k	ϕ	lit.
R0	$NH_2^* + M \rightarrow NH_2 + M$	2.0×10^{10}		*b*
R1a	$NH_2 + NO \rightarrow N_2 + H_2O$	8.5×10^{12}	0.9	*b*, 39
R1b	$NH_2 + NO \rightarrow N_2 + OH + H$		0.1	*b*, 39
R2	$2NH_2 + M \rightarrow N_2H_4 + M$	1.0×10^{18}		40
R3a	$NH_2 + NH_2 \rightarrow N_2H_2 + H_2$	7.8×10^{11}		41
R3b	$NH_2 + NH_2 \rightarrow NH_3 + NH$	1.1×10^{09}		42
R4	$NH_2 + H + M \rightarrow NH_3 + M$	1.1×10^{18}		43
R5	$NH_2 + H \rightarrow NH + H_2$	1.8×10^{07}		*c*
R6	$NH_2 + OH \rightarrow NH_2OH$	5.6×10^{13}		45
R7	$NH_2 + OH \rightarrow NH + H_2O$	1.0×10^{12}		46
R8	$NH_3 + H \rightarrow NH_2 + H_2$	6.2×10^{03}		47
R9	$NH_3 + OH \rightarrow NH_2 + H_2O$	9.1×10^{10}		39
R10	$H + H + M \rightarrow H_2 + M$	2.2×10^{15}		48

[a] Supplement reactions of the excited NH_2^* analogous to reactions R1−R7 are not listed but were taken into account by assuming the same rate constants as those for the thermally equilibrated NH_2. $T = 295$ K; k, rate constants in units of cm^3, mol, and s; ϕ, branching fraction. [b] This work. [c] Estimated based on ref 44.

From five experiments, the following rate constants were determined for reactions R0 and R1:

$$k_0 = (1.98 \pm 0.11) \times 10^{10}\ \text{cm}^3\ \text{mol}^{-1}\ \text{s}^{-1}$$

$$k_1 = (8.00 \pm 0.55) \times 10^{12}\ \text{cm}^3\ \text{mol}^{-1}\ \text{s}^{-1}$$

The stated errors correspond to the errors of the means based on a 2σ confidence level. Furthermore, consistent values of the initial concentration of NH_2 were obtained which are in very good agreement with estimated values based on the photolysis yield within 15%. Actually, the absence of sensitive secondary reactions suggests that the final rate constant depends little on the exact $[NH_2^*]_0$ value assumed and the predominant influence of reaction R2 at long reaction times makes a pseudo-first-order evaluation feasible. Such an analysis, which was restricted to reaction times >100 μs, is exemplarily shown in the small inset graph in Figure 11. Overall, this more approximate evaluation yielded a somewhat lower rate constant of $k_1 = (7.64 \pm 0.78) \times 10^{12}$ cm^3 mol^{-1} s^{-1}.

4.3.3. Comparison. The obtained rate constants based on the eSKaR measurements, $k_1 = (8.53 \pm 0.70) \times 10^{12}$ cm^3 mol^{-1} s^{-1}, and the conventional pump−probe experiment, $k_1 = (8.00 \pm 0.55) \times 10^{12}$ cm^3 mol^{-1} s^{-1}, agree well within their error limits. Since both experiments have been performed using the same experimental setup and differ solely by adjusting the excess ratio of [NO]/[NH_2], this agreement can be taken as a direct validation of the eSKaR method.

The obtained rate constant, which may be, in principle, still affected by systematic errors, can be further verified by a comparison with literature data. For this comparison, we take the eSKaR result, since it is based on a more comprehensive data set. Due to the importance of the reaction, 22 direct room

temperature measurements can be found in the literature. The reported rate constants are scattered over the range $4.1 < k_1/(10^{12}\ \mathrm{cm^3\ mol^{-1}\ s^{-1}}) < 16$. It is beyond the scope of this paper to review all these studies, and thus, we refer to the latest IUPAC recommendation, $k_1 = (9.7 \pm 3.5) \times 10^{12}\ \mathrm{cm^3\ mol^{-1}\ s^{-1}}$, which represents the mean of 20 studies. The large error limit set by the authors is due to an unsolved systematic discrepancy between values of the rate coefficients obtained in pulsed photolysis studies and those obtained using the discharge flow technique, which are significantly lower. Including the results of two additional discharge flow studies of Gersh et al.[37] and Jeffries et al.,[38] a little lower mean of $k_1 = (9.2 \pm 1.2) \times 10^{12}\ \mathrm{cm^3\ mol^{-1}\ s^{-1}}$ is obtained. Here, the error limits correspond to the error of the mean based on a 2σ confidence level. The good agreement of this averaged value with our result underlines the absolute accuracy of the eSKaR method.

Finally, including an additional uncertainty of 3% related to the absolute NO concentration due to mixture preparation, the following rate constant is recommended:

$$k_1 = (8.5 \pm 1.0) \times 10^{12}\ \mathrm{cm^3\ mol^{-1}\ s^{-1}}$$

5. Conclusion

Using the rate constant of the reaction $NH_2 + NO$ as the validation target, the extended simultaneous kinetics and ring-down (eSKaR) model has been shown to provide a reliable method for extracting rate constants from nonexponential cavity ringdown profiles that arise from a convolution of the ensuing reactions with the interfering bandwidth effect. The eSKaR method thus extends the applicability of CRDS to measurements of fast reactions of small radicals using conventional pulsed dye lasers as the probe light source.

To account for the bandwidth effect, the line shapes of the probe laser and the absorption line of the detected species have to be known. Detailed line shape measurements have been performed to ensure a proper treatment of the bandwidth effect. Small line shape inaccuracies, however, were shown to induce only minor errors in the finally determined rate constant, and thus, the eSKaR method is suitable for routine kinetics measurements without too demanding additional experimental (line shape measurements) and data reduction (eSKaR evaluation) efforts. Overall, the comparison of the line width data with narrow-bandwidth absorption data as well as the determination of the rate constant by means of two different experimental approaches (eSKaR and conventional pump−probe experiments) add up to a completely consistent picture for all measured quantities.

On the basis of the eSKaR measurements, the room temperature rate constant of the reaction $NH_2 + NO \rightarrow$ products has been found to be

$$k_1(T = 295\ \mathrm{K}) = (8.5 \pm 1.0) \times 10^{12}\ \mathrm{cm^3\ mol^{-1}\ s^{-1}}$$

The pressure broadening coefficient of NH_2 at room temperature

$$\Delta\nu_p^\circ = 2.27\ \mathrm{GHz/bar}$$

has been determined, where NH_2 radicals have been detected in the $\tilde{A}\ ^2A_1(090) \leftarrow \tilde{X}^2B_1(000)\Sigma$ band at wavelengths around $\lambda \approx 597$ nm.

Acknowledgment. This work was supported by the Deutsche Forschungsgemeinschaft. G.F. thanks R. Signorell, M. Suhm, J. Troe, and H. Gg. Wagner for making the ring-dye laser system available, which played a decisive role in this study.

References and Notes

(1) O'Keefe, A.; Deacon, D. A. G. *Rev. Sci. Instrum.* **1988**, *59*, 2544.
(2) Busch, K. W.; Busch, M. A. *Cavity Ringdown Spectroscopy—An Ultratrace-Absorption Measurement Technique*; ACS Symposium Series; Oxford University Press: Washington, DC, 1999; Vol. 720.
(3) Berden, G.; Peeters, R.; Meijer, G. *Int. Rev. Phys. Chem.* **2000**, *19*, 565.
(4) Kessels, W. M. M.; Hoefnagels, J. P. M.; van den Oever, P. J.; Barrell, Y.; van den Sanden, M. C. M. *Surf. Sci.* **2003**, *547*, 865.
(5) Macko, P.; Bánó, G.; Hlavenka, P.; Pla×f0il, R.; Poterya, V.; Pysanenko, A.; Votava, O.; Johnson, R.; Glosík, J. *Int. J. Mass. Spectrosc.* **2004**, *233*, 299.
(6) Yu, T.; Lin, M. C. *J. Am. Chem. Soc.* **1993**, *115*, 4371.
(7) Yu, T.; Lin, M. C. *J. Am. Chem. Soc.* **1994**, *116*, 9571.
(8) Diau, E. W.; Yu, T.; Wagner, M. A. G.; Lin, M. C. *J. Phys. Chem.* **1994**, *98*, 4034.
(9) Atkinson, D. B.; Hudgens, J. W. *J. Phys. Chem. A* **1997**, *101*, 3901.
(10) Atkinson, D. B.; Hudgens, J. W. *J. Phys. Chem. A* **1999**, *103*, 4242.
(11) Brown, S. S.; Ravishankara, A. R.; Stark, H. *J. Phys. Chem. A* **2000**, *104*, 7044; **2000**, *104*, 8600.
(12) Czyżewski, A.; Ernst, K.; Franssen, G.; Karasinski, G.; Kmieciak, M.; Lange, H.; Skubiszak, W.; Stacewicz, T. *Chem. Phys. Lett.* **2002**, *357*, 477.
(13) Yalin, A. P.; Zare, R. N.; Laux, C. O.; Kruger, C. H. *Appl. Phys. Lett.* **2002**, *81*, 1408.
(14) Jongma, R. T.; Boogaarts, M. G. H.; Holleman, I.; Meijer, G. *Rev. Sci. Instrum.* **1995**, *66*, 2821.
(15) Zalicki, P.; Zare, R. N. *J. Chem. Phys.* **1995**, *102*, 2708.
(16) Hodges, J. T.; Looney, J. P.; van Zee, R. D. *Appl. Opt.* **1996**, *35*, 4112.
(17) Newman, S. M.; Lane, I. C.; Orr-Ewing, A. J.; Newnham, D. A.; Ballard, J. *J. Chem. Phys.* **1999**, *110*, 10749.
(18) Mercier, X.; Therssen, E.; Pauwels, J.; Desgroux, P. *Combust. Flame* **2001**, *125*, 656.
(19) Guo, Y. Q.; Fikri, M.; Friedrichs, G.; Temps, F. *Phys. Chem. Chem. Phys.* **2003**, *5*, 4622.
(20) Chu, J. O.; Beach, D. B.; Estes, R. D.; Jasinski, J. M. *Chem. Phys. Lett.* **1988**, *143*, 135.
(21) Gehring, H.; Hoyermann, K.; Schacke, H.; Wolfrum, J. *Proc. Combust. Inst.* **1972**, *14*, 99.
(22) Miller, J. A.; Bowman, C. T. *Prog. Energy Combust. Sci.* **1989**, *15*, 287.
(23) Glarborg, P.; Miller, J. A. *Int. J. Chem. Kinet.* **1999**, *31*, 757.
(24) Lesclaux, R.; Khe, P. V.; Dezauzier, P.; Soulignac, J. C. *Chem. Phys. Lett.* **1975**, *35*, 493.
(25) Lehmann, K. K.; Romanini, D. *J. Chem. Phys.* **1996**, *105*, 10263.
(26) Hodges, J. T.; Looney, J. P.; van Zee, R. D. *J. Chem. Phys.* **1996**, *105*, 10278.
(27) McIlroy, A.; Jeffries, J. B. *Applied Combustion Diagnostics*; Kohse-Höinghaus, K., Jeffries, J. B., Eds.; Taylor and Francis: New York, 2002.
(28) Fikri, M. Zeitaufgelöste Cavity-Ringdown-Messungen der Druckabhängigkeit der Reaktionen von SiH_2-Radikalen mit O_2 und den Alkenen C_2H_4, C_3H_6 und *trans*-C_4H_8. Ph.D. Thesis, Universität Kiel, 2004.
(29) Brown, S. S.; Stark, H.; Ravishankara *Appl. Phys. B* **2002**, *75*, 173.
(30) Halpern, J. B.; Hancock, G.; Lenzi, M.; Welge, K. H. *J. Chem. Phys.* **1975**, *63*, 4808.
(31) Chen, F. Z.; Judge, D.; Wu, C. Y. R.; Caldwell, J. *Planet Space Sci.* **1999**, *47*, 261.
(32) Kohse-Höinghaus, K.; Davidson, D. F.; Chang, A. Y.; Hanson, R. K. *J. Quant. Spectrosc. Radiat. Transfer* **1989**, *42*, 1.
(33) Wachsmuth, U.; Abel, B. *J. Geophys. Res.* **2003**, *108*, 4473.
(34) Romanini, D.; Lehmann, K. K. *J. Chem. Phys.* **1993**, *99*, 6287.
(35) Votsmeier, M.; Song, S.; Davidson, D. F.; Hanson, R. K. *Int. J. Chem. Kinet.* **1999**, *31*, 323.
(36) Kee, R. J.; Ruply, F. M.; Miller, J. A. *Chemkin-II: A Fortran Chemical Kinetics Package for the Analysis of Gas-Phase Chemical Kinetics*, Sandia Report SAND89-8009, Sandia National Laboratories, Livermore, California, 1989, http://www.ca.sandia.gov/chemkin/.
(37) Gersh, M. E.; Silver, J. A.; Zahniser, M. S.; Kolb, C. E.; Brown, R. G.; Gozewski, C. M.; Kallelis, S.; Wormhoudt, J. C. *Rev. Sci. Instrum.* **1981**, *52*, 1213.
(38) Jeffries, J. B.; McCaulley, J. A.; Kaufman, F. *Chem. Phys. Lett.* **1984**, *106*, 111.
(39) Atkinson, R.; Baulch, D. L.; Cox, R. A.; Hampson, R. F. J.; Kerr, J. A.; Rossi, M. J.; Troe, J. *J. Phys. Chem. Ref. Data* **1997**, *26*, 1329.
(40) Khe, P. V.; Soulignac, J. C.; Lesclaux, R. *J. Phys. Chem.* **1977**, *81*, 210.
(41) Stothard, N.; Humpfer, R.; Grotheer, H.-H. *Chem. Phys. Lett.* **1995**, *240*, 474.

(42) Xu, Z. F.; Fang, D. C.; Fu, X. Y. *Int. J. Quantum. Chem.* **1998**, *70*, 321.
(43) Schofield, K. *J. Phys. Chem. Ref. Data* **1973**, *2*, 25.
(44) Röhrig, M.; Wagner, H. Gg. *Proc. Combust. Inst.* **1994**, *25*, 975.
(45) Fagerström, K.; Jodkowski, J. T.; Lund, A.; Ratajczak, E. *Chem. Phys. Lett.* **1995**, *236*, 103.
(46) Cohen, N.; Westberg, K. R. *J. Phys. Chem. Ref. Data* **1991**, *20*, 1211.
(47) Friedrichs, G.; Wagner, H. Gg. *Z. Phys. Chem.* **2000**, *214*, 1151.
(48) Baulch, D. L.; Cobos, C. J.; Cox, R. A.; Esser, C.; Frank, P.; Just, T.; Kerr, J. A.; Pilling, M. J.; Troe, J.; Walker, R. W.; Warnatz, J. *J. Phys. Chem. Ref. Data* **1992**, *21*, 411.